

Molecular ions in L 1544. I. Kinematics

P. Caselli , C. M. Walmsley,

and

A. Zucconi

Osservatorio Astrofisico di Arcetri, Largo E. Fermi 5, I-50125 Firenze, Italy;

caselli@arcetri.astro.it; walmsley@arcetri.astro.it; zucconi@arcetri.astro.it

M. Tafalla

Observatorio Astronómico Nacional (IGN), Campus Universitario, E-28800 Alcalá de Henares

(Madrid), Spain; tafalla@oan.es

L. Dore

Dip. Chimica "Ciamincian", Università di Bologna, Via Selmi 2, I-40126, Bologna, Italy;

dore@ciam.unibo.it

and

P. C. Myers

Harvard-Smithsonian Center for Astrophysics, MS 42, 60 Garden Street, Cambridge, MA 02138,

U.S.A.; pmyers@cfa.harvard.edu

ABSTRACT

We have mapped the dense dark core L 1544 in $\text{H}^{13}\text{CO}^+(1-0)$, $\text{DCO}^+(2-1)$, $\text{DCO}^+(3-2)$, $\text{N}_2\text{H}^+(1-0)$, $\text{N}_2\text{H}^+(3-2)$, $\text{N}_2\text{D}^+(2-1)$, $\text{N}_2\text{D}^+(3-2)$, $\text{C}^{18}\text{O}(1-0)$, and $\text{C}^{17}\text{O}(1-0)$ using the IRAM 30-m telescope. We have obtained supplementary observations of $\text{HC}^{18}\text{O}^+(1-0)$, $\text{HC}^{17}\text{O}^+(1-0)$, and $\text{D}^{13}\text{CO}^+(2-1)$. Many of the observed maps show a general correlation with the distribution of dust continuum emission in contrast to $\text{C}^{18}\text{O}(1-0)$ and $\text{C}^{17}\text{O}(1-0)$ which give clear evidence for depletion of CO at positions close to the continuum peak. In particular $\text{N}_2\text{D}^+(2-1)$ and $(3-2)$ and to a lesser extent $\text{N}_2\text{H}^+(1-0)$ appear to be excellent tracers of the dust continuum. Our DCO^+ maps have the same general morphology as the continuum while $\text{H}^{13}\text{CO}^+(1-0)$ is more extended. We find also that many apparently optically thin spectral lines such as HC^{18}O^+ and D^{13}CO^+ have double or highly asymmetric profiles towards the dust continuum peak. We have studied the velocity field in the high density nucleus of L 1544 putting particular stress on tracers such as N_2H^+ and N_2D^+ which trace the dust emission and which we therefore believe trace the gas with density of order of 10^5 cm^{-3} . We find that the tracers of high density gas (in particular N_2D^+) show a velocity gradient along the minor axis of the L 1544 core and that there is evidence for larger linewidths close to the dust emission peak. We interpret this using

the model of the L 1544 proposed by Ciolek and Basu 2000 and by comparing the observed velocities with those expected on the basis of their model. The results show reasonable agreement between observations and model in that the velocity gradient along the minor axis and the line broadening toward the center of L 1544 are predicted by the model. This is evidence in favour of the idea that amipolar diffusion across field lines is one of the basic processes leading to gravitational collapse. However, the double-peaked nature of the profiles is reproduced only at the core center and if a “hole” in the molecular emission, due to depletion, is present. Moreover, line widths are significantly narrower than observed and are better reproduced by the Myers & Zweibel 2001 model which considers the quasistatic vertical contraction of a layer due to dissipation of its Alfvénic turbulence, indicating the importance of this process for cores in the verge of forming a star.

Subject headings: ISM: individual (L 1544) – ISM: dust, extinction – ISM: molecules

1. Introduction

A considerable amount of observational work has gone into the study of “prestellar cores” (sometimes called pre-protostellar cores) which are dense condensations within molecular clouds which are thought to be on the point of collapse (see e.g. André et al. 2000). Such objects are found observationally to be extremely cold (< 15 K) and with column densities much higher than the surrounding molecular clouds. They also occasionally show evidence for infall (Tafalla et al. 1998) and an example of this is the high density core associated with L 1544. One concludes therefore that such objects are close to being in the “pivotal state” from which gravitational collapse can commence. Determining their density distribution and kinematic properties is thus a matter of great interest.

The density distribution in “starless cores” has been delineated both by the observed dust emission and extinction as well as in molecular line maps. The latter however appear in many cases to give an inaccurate picture of the true column density distribution due to the fact that at the temperatures of the pre-stellar cores, much of the molecular gas is depleted out onto dust grains. The dust emission/extinction data (e.g Ward-Thompson et al. 1999 (hereafter WMA), Bacmann et al. 2000 (hereafter BAP), Alves et al. 2001) show that starless cores have molecular hydrogen column densities ranging up to 10^{23} cm $^{-2}$ equivalent to 100 magnitudes of visual extinction. There is evidence for a column density profile varying as a function of offset from the central position R as $1/R$ but with a flatter profile below a critical radius of roughly 3000 AU. This is reminiscent of the structures expected in hydrostatic equilibrium such as a “Bonnor-Ebert sphere” and indeed recent NIR extinction data for B68 show impressive agreement with the distribution expected for such a sphere (Alves et al. 2001). However, it is clear that reality is more complicated since the

contours of dust emission/absorption as a rule are far from being spherically symmetric. This suggests that magnetic fields play an important role in the dynamics of such systems.

Models for the likely magnetic field structures in cores in quasi-hydrostatic equilibrium have been constructed by a variety of authors (see e.g. Shu et al. 1987, Ciolek and Basu 2000 (hereafter CB00), Ciolek and Basu 2001 and references therein). These vary in detail but have in common the idea that ambipolar diffusion across magnetic field lines permits collapse on a time scale roughly an order of magnitude longer than the free-fall time. In this case, one expects a “disk-like” structure and for the particular case of L 1544, it has been shown (CB00) that the observed dust column density distribution is in reasonable agreement with the model column density distribution just prior to collapse. In their model, the observed “disk” is almost edge-on (inclined at an angle of 16°) and is contracting radially in the plane of the disk. Recently, Myers & Zweibel 2001 (hereafter MZ) have studied a flattened cloud in quasistatic vertical contraction triggered by Alfvénic turbulence dissipation. As we will see, this model also reproduces some of the features observed towards L 1544.

Understanding the kinematics in cores such as L 1544 clearly requires observation of molecular lines. The results of Caselli et al. 1999 (see also Caselli & Walmsley 2001) show clearly however that CO and its isotopically substituted counterparts are depleted onto dust grain surfaces at densities above 10^5 cm^{-3} in L 1544. Observations of other cores (Tafalla et al., in prep.) show a very similar picture. However it is clear that certain species and, in particular N_2H^+ , have a spatial distribution which is much more similar to that of the dust than CO. The natural inference is that these species, or perhaps species to which they are chemically linked, are either undepleted or much less depleted than CO at high densities. In the particular case of N_2H^+ , it is known chemically to be linked to molecular nitrogen which is likely to be the main repository of nitrogen in the gas phase. N_2 is somewhat more volatile than CO and hence it is plausible that there are situations where N_2 is undepleted and CO is in solid form (see e.g. Bergin & Langer 1997). This has the consequence that the kinematics of dense gas in starless cores such as L 1544 will be best delineated by species such as N_2H^+ and chemically related molecules (e.g. N_2D^+). One of the objectives of the present study is to test current models of the contraction of L 1544 exploiting this fact.

L 1544 consists of a dense core surrounded by a low density envelope which causes self-absorption of many transitions emitted by the dense gas. This self-absorption is a considerable problem for studies aimed at determining the characteristics of the denser material. The $\text{N}_2\text{H}^+(1-0)$ transition shows evidence for absorption (Williams et al. 1999) by a foreground layer of density roughly 10^4 cm^{-3} which is red-shifted by 0.1 km s^{-1} . This foreground absorption is a complication for those interested in the kinematics of the dense gas and there are therefore advantages to be gained in observing higher J transitions of N_2H^+ and analogous species for which it is likely that the foreground absorption will be either absent or very weak.

In the present article, we describe a study of L 1544 carried out in a variety of molecular

transitions. We have concentrated on the emission of molecular ions because a main aim of the study has been to determine the ionization degree as a function of position within the dense nucleus of L 1544. This parameter essentially determines the ambipolar diffusion time scale and hence the timescale for star formation. A companion paper to the present article (Caselli et al. 2001b, hereafter Paper II) concerns itself with the determination of the ionization degree and the chemistry of the high density gas in L 1544. In this article, we present the data and discuss what conclusions can be drawn about the kinematics of the dense gas. We conclude by making a comparison of our data with that expected on the basis of models of core evolution.

Observations are described in Section 2 and our principal observational results are discussed in Section 3. In Section 4, we compare with the models of CB00 and MZ and discuss the outcomes. In section 5, we summarize our conclusions.

2. Observations

The data described here were taken using the IRAM 30-m telescope in three sessions: January 1997, August 1997, November 1998, and July 2000. We in general observed using simultaneously the three facility receivers at 3, 2, and 1.3mm. Part of the $\text{N}_2\text{H}^+(1-0)$ data reported and analysed in this paper have been already presented in Tafalla et al. 1998. We now give a brief description of each session.

2.1. H^{13}CO^+ and DCO^+ map from January 1997

In January 1997, we observed simultaneously $\text{H}^{13}\text{CO}^+(1-0)$, $\text{DCO}^+(2-1)$, and $\text{DCO}^+(3-2)$. The corresponding half power beamwidths were $28''$, $17''$, and $11''$ at 3, 2, and 1.3mm, respectively. We observed a map of 67 positions with a grid spacing of $20''$ relative to our reference position $\text{R.A.}(1950) = 05^{\text{h}}01^{\text{m}}11.0^{\text{s}}$, $\text{Dec.}(1950) = 25^{\circ}07'00''$. We observed in frequency switching mode with a frequency throw of 1.0, 1.5, and 2.0 MHz at 3, 2, and 1mm, respectively. The pointing was checked at 1-2 hourly intervals by means of a 3mm continuum scan on the nearby quasar 0528+134 and is thought to be good to $\sim 4''$. The relative pointing of the three receivers was checked observing Mars and was found to be accurate to within $2''$.

The backend for these observations was the facility autocorrelator split into three parts of bandwidth 20, 20, and 40 MHz at 3, 2, and 1mm, respectively. The corresponding spectral resolutions were 0.033 km s^{-1} for $\text{H}^{13}\text{CO}^+(1-0)$, 0.041 km s^{-1} for $\text{DCO}^+(2-1)$, and 0.054 km s^{-1} for $\text{DCO}^+(3-2)$.

2.2. August 1997 Observations of $\text{HC}^{18}\text{O}^+(1-0)$, $\text{D}^{13}\text{CO}^+(2-1)$, $\text{C}^{17}\text{O}(2-1)$, $\text{C}^{18}\text{O}(1-0)$, $\text{C}^{18}\text{O}(2-1)$, and $\text{HC}_3\text{N}(15-14)$

In August 1997, we observed using two different set-ups. In both, we observed simultaneously at 3, 2, and 1.3 mm. In the first, we tuned to $\text{HC}^{18}\text{O}^+(1-0)$, $\text{D}^{13}\text{CO}^+(2-1)$, and $\text{C}^{17}\text{O}(2-1)$. In the second, we tuned to $\text{C}^{18}\text{O}(1-0)$, $\text{HC}_3\text{N}(15-14)$, and $\text{C}^{18}\text{O}(2-1)$. The basic observational procedure was as described above for the January observations. These observations furnished a tentative detection of $\text{D}^{13}\text{CO}^+(2-1)$ which was then re-observed in the successive observing run. The $\text{C}^{17}\text{O}(2-1)$ data were of poor quality due to the high humidity and were discarded. The $\text{HC}_3\text{N}(15-14)$ line was detected and was further mapped in our July(2000) measurements (see below). HC_3N data will be presented in a separated paper (Comito et al., in prep).

2.3. November 1998 observations of $\text{HN}^{15}\text{N}^+(1-0)$, $\text{HC}^{17}\text{O}^+(1-0)$, $\text{D}^{13}\text{CO}^+(2-1)$, $\text{C}^{17}\text{O}(1-0)$, $\text{N}_2\text{D}^+(2-1)$, $\text{C}^{17}\text{O}(2-1)$

In November 1998, we observed the 1–0 transition of (i) HN^{15}N^+ and (ii) $\text{HC}^{17}\text{O}^+(1-0)$ together with the 2–1 transition of D^{13}CO^+ . In a second set-up, we observed the 1–0 and 2–1 lines of C^{17}O together with the 2–1 transition of N_2D^+ . The 1.3 mm data had to be discarded for technical reasons. The 1–0 transition of HN^{15}N^+ was not detected at offset (20'', -20'') down to a limit of 0.047 K.

2.4. July 2000 Observations of $\text{N}_2\text{H}^+(3-2)$, $\text{N}_2\text{D}^+(2-1)$, and $\text{N}_2\text{D}^+(3-2)$

On July 8–10, we observed L 1544 in $\text{N}_2\text{H}^+(1-0)$, $\text{HC}_3\text{N}(15-14)$, $\text{N}_2\text{D}^+(2-1)$, $\text{N}_2\text{D}^+(3-2)$, and $\text{N}_2\text{H}^+(3-2)$. The spectral resolutions were as follows : 0.038 km s^{-1} , 0.051 km s^{-1} , and 0.042 km s^{-1} at the frequencies of $\text{N}_2\text{D}^+(2-1)$, $\text{N}_2\text{D}^+(3-2)$, and $\text{N}_2\text{H}^+(3-2)$, respectively. System temperatures (corrected for the atmosphere) were $\sim 120 \text{ K}$ for $\text{N}_2\text{H}^+(1-0)$, $\sim 250 \text{ K}$ for $\text{N}_2\text{D}^+(2-1)$, $\sim 350 \text{ K}$ for $\text{N}_2\text{D}^+(3-2)$, and $\sim 600 \text{ K}$ for $\text{N}_2\text{H}^+(3-2)$ observations. The HPBW was $16''$ for $\text{N}_2\text{D}^+(2-1)$, $10''$ for $\text{N}_2\text{D}^+(3-2)$, and $9''$ for $\text{N}_2\text{H}^+(3-2)$.

3. Observational Results

In this section we give an overview of our observational results. We first consider the line profiles observed towards our (20,-20) offset. This is close to the high density peak in the L 1544 discussed by WMA and by BAP. We will refer to it in the following as the dust emission peak. We then present our maps of integrated intensity in $\text{H}^{13}\text{CO}^+(1-0)$, $\text{DCO}^+(2-1)$, $\text{DCO}^+(3-2)$, $\text{N}_2\text{H}^+(1-0)$, $\text{N}_2\text{D}^+(2-1)$, and $\text{N}_2\text{D}^+(3-2)$ and compare with the dust emission maps. These comparisons allow us to extend and confirm the conclusion of Caselli et al. 1999 (hereafter

CWT99) that whereas CO isotopomers are underabundant in the high density peak of L 1544, certain ionic species remain relatively abundant.

3.1. Spectra towards the dust emission peak

In Fig. 1, we present spectra towards the (20,-20) offset in L 1544 and in Table 2 we present gaussian fit results for these spectra. The form of these spectra has some importance for the later discussion and we therefore lay some emphasis on it here. In the first place, as has been discussed by many authors (e.g. Tafalla et al. 1998, Williams et al. 1999, CWT99), many of the observed profiles are double-peaked and as a consequence are fit by two gaussian components in Table 2. This could *a priori* be interpreted as implying two layers with different velocities along the line of sight but another interpretation is that, at least for the more abundant species, the observed profiles are affected by absorption in a low density (10^4 cm^{-3}) foreground layer which is at red-shifted velocities (0.08 km s^{-1}) relative to the high density core (see e.g. Williams et al. 1999).

If this latter view is correct, one expects to see the effects of foreground absorption in low excitation lines of abundant species. Optically thin lines should show weaker single peaked features. However, our data show clearly that even weak lines of low abundance species such as $\text{D}^{13}\text{CO}^+(2-1)$, $\text{HC}^{18}\text{O}^+(1-0)$, $\text{HC}^{17}\text{O}^+(1-0)$ (see Dore et al. 2001), and $\text{DCO}^+(3-2)$ appear double with component separations between 0.24 and 0.27 km s^{-1} and individual component widths between 0.2 and 0.27 km s^{-1} . It is also important that there are slight offsets of order 0.05 km s^{-1} (15 kHz at 3mm) between the measured velocities for different species. It seems possible to us that this is due to the uncertainties in the spectroscopic constants but this requires verification. In the case of $\text{HC}^{17}\text{O}^+(1-0)$, the uncertainty in the measured frequency is 20 kHz (Dore et al. 2001), corresponding to 0.07 km s^{-1} , which accounts for the observed velocity shift between this line and $\text{HC}^{18}\text{O}^+(1-0)$ (see Fig. 1 and Tab. 2). Thus either there are two high density velocity components along the line of sight (and the transitions mentioned above are optically thin) or there are very high abundances of HCO^+ and DCO^+ in the postulated foreground layer allowing foreground absorption even in $\text{D}^{13}\text{CO}^+(2-1)$ and $\text{HC}^{17}\text{O}^+(1-0)$. The former is in agreement with the conclusions derived from C^{34}S by Tafalla et al. 1998 and seems to us more likely.

Another reason is the recent detection of the three hyperfine components of $\text{HC}^{17}\text{O}^+(1-0)$ at 87057.23 MHz (Dore et al. 2001). It is noticeable that the form of the $\text{HC}^{17}\text{O}^+(1-0)$ profile (albeit with moderate S/N) is similar to that of $\text{HC}^{18}\text{O}^+(1-0)$ as one would expect if both were optically thin. Indeed, the intensity ratio is equal to 3 ± 1 and 5 ± 1 for the blue and red components, respectively, close to the $[\text{}^{18}\text{O}]/[\text{}^{17}\text{O}]$ abundance ratio in the local interstellar medium ($= 3.65$, Penzias 1981). We conclude from this that $\text{HC}^{18}\text{O}^+(1-0)$ is likely to be optically thin and thus that the double nature of the profile is in this case due to the existence of two velocity components along the line of sight. Thus, foreground absorption seems improbable in this case.

This does not imply that “self-absorption effects” are unimportant. On the contrary, our profile of $\text{H}^{13}\text{CO}^+(1-0)$ is clearly broader with a larger separation between peaks (0.36 km s^{-1}) than in $\text{HC}^{18}\text{O}^+(1-0)$ and it is probable that $\text{H}^{13}\text{CO}^+(1-0)$ is optically thick. And there are differences in the profiles of different hyperfine components of $\text{N}_2\text{H}^+(1-0)$ which suggest to us that while most components are self-absorbed, the weakest $F_1, F = 1, 0 \rightarrow 1, 1$ component is close to being thin ($\tau_{1,0-1,1} \lesssim 0.7$). For this reason, we sometimes have used the observations of this component to derive column densities of N_2H^+ (see Paper II). In general also, we conclude that observations of weak $< 1 \text{ K}$ lines of low abundance species are optically thin and can be used for column density determination. They appear often to be double-peaked towards the high density core of L 1544 and this is most simply interpreted as implying two separate velocity components along the line of sight. In Section 4 we discuss these components as arising from a combination of contraction and depletion.

3.2. N_2H^+ and N_2D^+ spectra

We discuss separately our July 2000 spectra of $\text{N}_2\text{H}^+(3-2)$ and $\text{N}_2\text{D}^+(2-1)$ and $(3-2)$ because there are few observations of these transitions available to date in such cold starless cores. Moreover, we expect these high J transitions to sample preferentially regions of high density within the L 1544 core. Interpretation of the spectra is complicated by the hyperfine structure of these transitions. $\text{N}_2\text{H}^+(3-2)$ for example has 45 components spread out over roughly 6 km s^{-1} . $\text{N}_2\text{D}^+(2-1)$ has 38 components spread over 10 km s^{-1} . Although many of these components have negligible intensity, most of the structure which we observe in Fig. 2 is due to hyperfine splitting. This is an advantage in that it permits a direct determination of optical depth based on the satellite line intensities but it makes it extremely difficult to infer the line profile in the region of line formation.

We demonstrate this by showing in Fig. 2 our observed profiles at the molecular peak and the fits which we have made to the hyperfine structure. The frequencies used for the fit are discussed in appendix A (see also the recent discussion of Gerin et al. 2001 for N_2D^+). These fits assume constant excitation temperature for all of the hyperfine-split transitions and estimate the total optical depth of a hypothetical unsplit transition. Table 3 summarizes the line parameters at offset (20,-20). We note that $\text{N}_2\text{H}^+(1-0)$ and $\text{N}_2\text{D}^+(2-1)$ are clearly optically thick and we exploit this fact in the column density determinations discussed in Paper II.

Because of the fact that we expect these transitions to probe the dense portion of the L 1544 core, it is of interest to study their kinematics. Motions such as infall might give rise to wings on the observed profiles (Rawlings et al. 1992) and rotation of the dense core might cause a velocity gradient in the central region. The presence of blended hyperfine satellites however renders discussion of the intrinsic line profile extremely difficult.

3.3. Integrated Intensity Maps

Another useful input to the interpretation of the structure of the L 1544 high density core is given by the integrated intensity maps. CWT99 have already presented evidence that CO is depleted at densities above 10^5 cm^{-3} in L 1544. CWT99 also showed that the integrated intensity maps of at least some ionic species peaked near the WMA dust emission maximum. This is confirmed and extended by the maps shown in Fig. 3 where one sees that $\text{DCO}^+(2-1)$, $\text{DCO}^+(3-2)$, $\text{H}^{13}\text{CO}^+(1-0)$, and $\text{N}_2\text{D}^+(2-1)$ all peak close to the WMA 1.3mm maximum. This is most clear in $\text{N}_2\text{D}^+(2-1)$ for which the general features of our map are consistent with those of the dust emission. N_2D^+ is however more compact and we find for example half-power angular dimensions of $52'' \times 30''$ in $\text{N}_2\text{D}^+(2-1)$ as compared to $80'' \times 40''$ in the 1.3mm continuum map of WMA. The morphological similarities allow us to conclude that although CO and many other species are highly depleted in the vicinity of the dust emission maximum in L 1544, N_2D^+ and to a lesser extent N_2H^+ are not. Thus one can expect that N_2D^+ traces higher density material than CO and other depleted species. Indeed, N_2D^+ should probe the material within the region where the density (deduced from dust emission) becomes roughly constant.

On the other hand, we note that $\text{H}^{13}\text{CO}^+(1-0)$ is much more extended than N_2D^+ with a half-power size of order $100''$. Thus if we consider H^{13}CO^+ to be a tracer for the presence of CO in high density gas and N_2H^+ to be a tracer for N_2 , we conclude that CO is more depleted than N_2 at high densities. In both cases, the ions have higher dipole moments than the parent species (CO or N_2) to which they are linked chemically. They can thus trace the presence of these species in situations where direct detection is impossible (in the case of CO because of the effect of foreground and background emission). The fact that H^{13}CO^+ is much more extended than either the dust emission or N_2D^+ is a sign that CO is even more depleted in the central regions of L 1544 than would be implied by the observed C^{17}O column density.

We point out also that while the dust emission appears best traced by N_2D^+ , some other species have a rough correlation with the dust peak. DCO^+ peaks at a position slightly offset to the NW but has similar half-power contours to the dust. Several other species (HC_3N and NH_3 , Comito et al., in prep, Tafalla et al., in prep.) behave in analogous fashion. CS on the other hand (like the CO isotopomers) does not (see Tafalla et al. 1998). There thus appear to be two "families" of species (dust-peak-phobic and dust-peak philic) which are depleted and (relatively) undepleted respectively in the high density core of L 1544. In general, ions and deuterated species are "dust-peak-philic" and thus survive to some extent in the high density material (see also Bergin et al. 2001). To what extent this is borne out by quantitative analysis is seen in Paper II.

3.4. Velocity field

We analysed the velocity structure in the observed maps following the procedures in Goodman et al. 1993 to find a total velocity gradient for each tracer. We have also determined "local

gradients” based upon 9-point maps for $\text{H}^{13}\text{CO}^+(1-0)$, $\text{DCO}^+(2-1)$, $\text{DCO}^+(3-2)$, $\text{N}_2\text{H}^+(1-0)$, $\text{N}_2\text{D}^+(2-1)$, and $\text{N}_2\text{D}^+(3-2)$. We request that at least 7 neighbouring points are available for the local gradient fit. These results are presented in Fig. 4 where the velocity gradient vectors are superposed on the maps of integrated intensity shown in Fig. 3.

One sees in the first place that the observed velocity gradients indicate quite a complex velocity field in the high density core of L 1544. Also, there are distinct differences between the kinematics of different species with $\text{N}_2\text{D}^+(2-1)$ and $\text{N}_2\text{D}^+(3-2)$ having gradients predominantly along the minor axis of L 1544 while for other species, the situation is more complex. In the case of $\text{N}_2\text{H}^+(1-0)$, one sees that towards the west, vectors are mainly along the minor axis parallel to those observed in $\text{N}_2\text{D}^+(3-2)$ but towards the SE and E, the vectors are along the *major* axis. We believe that these same structures are being seen superposed in the H^{13}CO^+ and DCO^+ maps. However, there appears to be yet another feature on the NE of the $\text{DCO}^+(2-1)$ map with vectors along the minor axis but in the opposite direction to that seen in $\text{N}_2\text{D}^+(3-2)$. It is also noteworthy that the overall gradient seen in $\text{DCO}^+(2-1)$ of $1.2 \text{ km s}^{-1} \text{ pc}^{-1}$ along the major axis is rather similar to that reported by Ohashi et al. 1999 using CCS. This suggests that DCO^+ and CCS trace the same regions within the core. However, it seems doubtful to us that overall rotation is being traced as the gradient does not seem to be continuous. We conclude that $1.2 \text{ km s}^{-1} \text{ pc}^{-1}$ should be treated as an upper limit to the overall rotation rate. It is interesting to note that the direction of the total gradient as observed in $\text{DCO}^+(2-1)$ and $\text{N}_2\text{H}^+(1-0)$ lines is similar to the direction of the magnetic field as measured by Ward–Thompson et al. 2000.

It is a striking feature of our results that the lines which best trace the dust peak region (see Fig. 3) have their principal gradient along the minor axis of L 1544. If one assumes that the material close to the dust emission peak is that with the highest density, this implies that the high density gas has large velocity gradients along the L 1544 minor axis. Moreover, the velocity gradients seen in $\text{N}_2\text{D}^+(3-2)$ are the largest which we have detected suggesting that the high density gas is moving faster. It should be realised however that there are some *caveats* which must be applied to the above discussion. One of these is the errors in observed velocities due to radiation transport effects such as the foreground absorption discussed earlier. This however is unlikely to affect the high density material traced particularly well by $\text{N}_2\text{D}^+(3-2)$ where velocity gradients are as large as $7 \text{ km s}^{-1} \text{ pc}^{-1}$ and along the minor axis. An interesting feature of the $\text{N}_2\text{D}^+(3-2)$ emission map is its extension in the direction of the corresponding velocity gradient, in the opposite sense to that of the other line maps, in particular the 2–1 of the same species.

In a model where L 1544 has a “disk-like” structure seen almost edge-on, it is natural to attribute gradients along the minor axis to infall and gradients along the major axis to rotation. Indeed, Ohashi et al. 1999 claim evidence for both based on their CCS maps. The interesting point about our data however is that N_2D^+ , whose integrated intensity correlates well with the dust emission shows *only* evidence for infall. This suggests angular momentum loss between the scales where DCO^+ is abundant and those traced by N_2D^+ . We note also that the velocity gradients we estimate along the minor axis are considerably larger (between 3 and $7 \text{ km s}^{-1} \text{ pc}^{-1}$

in N_2D^+ than in CCS and DCO^+ along the major axis). If these latter estimates reflect real radial infall in the plane of the disk (inclination 16° according to CB00), they are affected by foreshortening and thus the gradient in the plane of the disk is between 0.9 and $2.1 \text{ km s}^{-1} \text{ pc}^{-1}$.

An alternative interpretation of the velocity pattern seen in $\text{N}_2\text{D}^+(3-2)$ might be rotation of a prolate core about its major axis. Although this is a possibility, it seems to us unlikely because this gradient, in the minor axis direction, is only seen on the small scales ($\sim 30''$) probed by N_2D^+ . At larger scales, the data indicate (if anything) a gradient along the major axis. Conservation of angular momentum might be expected to produce similarly oriented gradients in different density regimes. However, we cannot presently exclude the possibility of rotation in the central high density region, given the complex kinematics shown by the local gradients in Fig. 4.

3.5. Variation of line widths across the core

Another tracer of the velocity field in cores such as L 1544 is the observed line width. The discussion of the previous section had essentially to do with gradients in the centroid velocity in the plane of the sky. The measured line width in principle contains information about gradients in the line of sight of the centroid velocity. However, such effects are usually confused by both thermal line broadening and broadening due to local micro-turbulence and it is often difficult to distinguish the different contributions to observed profiles. In the present case however, the evidence that many observed profiles are non-gaussian is a strong indication that there are gradients also along the line of sight.

In Fig. 5, we show observed line widths of $\text{N}_2\text{H}^+(1-0)$, $\text{N}_2\text{D}^+(2-1)$, and $\text{N}_2\text{D}^+(3-2)$ plotted against the projected offset from the dust continuum peak. These line widths have been derived correcting for hyperfine blending and optical depth assuming emission from a layer of homogeneous excitation temperature and an intrinsically gaussian profile. In the case of N_2D^+ , the hyperfine blending effects are sufficiently large that departures from a gaussian profile would be extremely difficult to detect and hence the line width is the only useful parameter of the profile which can be derived. In the case of $\text{N}_2\text{H}^+(1-0)$ however, one clearly observes individual satellites with double-peaked profiles as has been discussed by various authors (Williams et al. 1999) but we have nevertheless fitted a single component for purposes of comparison with N_2D^+ .

Fig. 5 shows that the observed widths in $\text{N}_2\text{H}^+(1-0)$ are rather similar to $\text{N}_2\text{D}^+(2-1)$ and $\text{N}_2\text{D}^+(3-2)$ consistent with the lines being formed in the same region. Both in $\text{N}_2\text{H}^+(1-0)$ and in $\text{N}_2\text{D}^+(2-1)$, we see evidence for a slight fall-off of line widths from values of order 0.3 km s^{-1} close to the dust emission peak. There is no evidence in these data for an increase at large distances from the core nucleus as expected in some models where magneto-hydrodynamic waves are incident on the core exterior (see e.g. Goodman et al. 1998). On the contrary, there is evidence for increased line broadening towards the dust peak of L 1544. This is in qualitative agreement with infall (contraction) of the nucleus of L 1544.

Linewidths of $\text{DCO}^+(2-1)$ and $(3-2)$ are also plotted against the projected offset in Fig. 5. At large distances from the center, DCO^+ linewidths show more scatter than N_2H^+ and N_2D^+ linewidths, probably due to the more extended morphology. No correlations between DCO^+ linewidths and the distance from the $(20, -20)$ offset appear from the figure. This may in part be due to the larger optical depth of DCO^+ lines (which do not present hyperfine splitting) compared with N_2H^+ and N_2D^+ , and in part to the differential depletion between the precursors CO and N_2 (discussed in Paper II) which prevents DCO^+ to trace the dense and highly CO-depleted nucleus of L 1544 where infall motions are more prominent.

4. Models of the kinematics

In this section, we present two models of the kinematics of L 1544, based on models of CB00 and of MZ. Each model assumes a flattened structure of dense gas threaded by a perpendicular magnetic field, and that gravity drives the gas motions. The CB00 model assumes that the flattened structure is a cylindrically symmetric disk, and predicts the radially inward motion of gas in the disk plane due to ambipolar diffusion. The MZ model considers the quasistatic vertical contraction of the layer due to dissipation of its Alfvénic turbulence. We note that polarization measurements at $850\ \mu\text{m}$ across L1544 (Ward-Thompson et al. 2000) are in apparent disagreement with the picture adopted here (i.e. the magnetic field in the plane of the sky seems to be roughly parallel to the major axis), although they show some angle deviation and some depolarization toward the core center.

The MZ and CB00 models treat what might possibly be earlier and later stages of the same process, but they differ in their physical formulation and in their adopted parameters. MZ consider the pressure of Alfvén waves (McKee & Zweibel 1995) as a key element in the vertical support of the layer and the dissipation of these waves as the basis of the condensation motions. Their layer is magnetically critical, and they neglect the slower motions due to ambipolar diffusion in the plane of the layer. In contrast, CB00 consider a disk with no turbulence and a weaker field: the disk is magnetically supercritical by a factor greater than 2 for the conditions adopted here within the central beam radius ($12''$ or $0.008\ \text{pc}$) at time $2.7\ \text{Myr}$. The CB00 disk is centrally condensed in the horizontal plane while the MZ layer is horizontally uniform. The angle between the vertical axis of the model and the plane of the sky (θ) is 16° in CB00, estimated from the observed aspect ratio of the 1.3mm continuum map, and is chosen here to be 75° for good fit between our $\text{HC}^{18}\text{O}^+(1-0)$ data towards the $(20, -20)$ offset and the MZ model. Thus in the present comparison the CB00 disk has nearly "edge-on" horizontal motions while the MZ layer has more nearly "pole-on" vertical motions. In the MZ model, the velocity gradient observed along the minor axis (Sect. 3.4) may be interpreted as rotation of the layer about an axis in the plane of the sky. We use CB00 results to predict line profiles of $\text{N}_2\text{H}^+(1-0)$ across the core and compare with observations.

We first explain how we derive "model profiles" and then compare models with observations.

4.1. CB00 Synthetic Profiles

For purposes of simplicity, we have made a number of assumptions. In the first place, we have chosen here to present results based upon the particular model of CB00 which gives best agreement with the observed intensity distribution of mm and submm continuum (see also Zucconi et al. 2001). This is the model at time $t_3 = 2.66$ Myr when the central density is $n(\text{H}_2) = 4.37 \cdot 10^6 \text{ cm}^{-3}$. The density distribution in the mid-plane of this structure has been given by CB00 and it is supposed isothermal at a temperature of 12 K (though the discussion of Zucconi et al. 2001 and Evans et al. 2001 makes it clear that this is quite a crude approximation). Then the density distribution perpendicular to the disk mid-plane can be computed assuming hydrostatic equilibrium.

As far as the velocity field is concerned, we have again based our simulation on the results of Ciolek and Basu 2000 for the radial (cylindrical) velocity in the disk mid-plane. We then assume that this holds also (in cylindrical coordinates) above and below the plane. One should note that this velocity field goes to zero at both the origin and at large radii with a maximum infall velocity (at time t_3) of 0.12 km s^{-1} at radius 0.025 parsec. We have accordingly made a fit to the dependence of the radial velocity upon radius predicted for the ions at time t_3 by CB00 (their Fig.2) and assumed we can use this to estimate the column density of N_2H^+ in a certain velocity range integrated along an arbitrary line of sight across the disk. We thus can compute model profiles by determining the hydrogen column density in a given velocity range for all lines of sight across the model disk.

We have also run some models with a slight variation on the above procedure intended to simulate the fact that many species are depleted out in the high density nucleus of L 1544 (to a lesser extent even N_2H^+ is likely to be depleted). We assume a central “hole” in the density distribution for radii less than a critical value r_h (which may differ from one species to another). This has the consequence that lines of sight crossing the central hole have no contribution from the velocity range corresponding to the central region of L 1544. As one sees in Paper II, this is an extremely crude approximation but it is useful in order to understand how one might obtain “double-peaked” profiles towards the center of L 1544.

We have carried out this procedure for $r_h = 0.01 \text{ pc}$ (i.e. for the particular case of N_2H^+) and present the resultant model profiles in Fig. 6. Here we have convolved with a beam corresponding to $24''$ at a distance of 140 parsec and we show results for a disk inclined by 16° to the line of sight (i.e. close to edge-on). We note that we consider a thermal broadening when constructing these model profiles, assuming a gas temperature of about 10 K (as deduced from C^{17}O , C^{18}O , and NH_3 observations; see Paper II and Tafalla et al., in prep.), although spectra without thermal broadening are also shown in Fig. 6 for comparison. On the other hand we neglect microturbulences. We also are implicitly assuming optically thin conditions.

We see in Fig. 6 that along the major axis of this contracting disk, we see symmetrical profiles with width of order 0.2 km s^{-1} . There is also an indication of “double peaks”, which does

not go away in the central position even when thermal broadening is taken into account. This is, we stress, due to the fact that we are viewing the model disk roughly edge on (in fact if we increase substantially the inclination, the indication for double peaks disappears and the line widths are reduced). Along the minor axis on the other hand, profiles become asymmetric with blue shifts of roughly 0.1 km s^{-1} to the north (in the representation of Fig. 6) and correspondingly red shifts to the south. Clearly, one has symmetry about the major axis in this model whereas along “E-W lines” the profiles should not change. As discussed in the previous section, one expects in this type of model velocity gradients along the minor axis as in fact observed in N_2D^+ .

One final point worth noting with regard to this model is that it “naturally” produces line widths of the order of 0.2 km s^{-1} even without recourse to any local line broadening (see histograms in Fig. 6). Thus a significant fraction of the observed line width is probably due to systematic motions. The model also predicts larger line widths towards the dust peak, because of the larger infall speeds, and indeed this is observed (Sect. 3.5).

4.1.1. Comparison of CB00 model kinematics with observations of L 1544

We here make a comparison of predictions from our simulations of the CB00 model with observations. When doing this, we have *not* made any systematic effort to fine-tune the models to improve the agreement with observations. We have only varied the inclination at which the CB00 disk is viewed (as shown later).

In Fig. 7, we compare observed and model profiles (with a central hole) along minor axes of L 1544 using the “weak” (hence presumed optically thin) $F_1, F = 1, 0 \rightarrow 1, 1$ satellite of N_2H^+ as a tracer. The central hole has a radius of 0.01 parsec. This latter value corresponds to around 2000 AU which is roughly the radius at which species such as N_2 become depleted (see Paper II). One notes that the model profile at the (20,-20) offset has a clearly marked central dip, and that observed profiles have the same general characteristics as those of the model, in the sense that there is evidence for asymmetries to the blue (40,0) and red (0,-40) (the first moment of the $\text{N}_2\text{H}^+(1-0)$ intensity distribution changes by $+0.06 \text{ km s}^{-1}$ going from (40,0) to (0, -40)). However, the observed profiles are wider than those predicted by the model.

Model and observations do not match along the NW direction of the major axis (not shown), where $\text{N}_2\text{H}^+(1-0)$ lines continue to show double peaks up to a projected distance of $57''$ (or 0.04 pc) from the center, probably due to the particular morphology of L 1544 which is likely to be more complex than the assumed cylindrical symmetric model cloud. Indeed, the unconvolved velocity profiles in Fig. 6 (see histograms) show two peaks along the major axis of the model cloud, although their separation is not sufficiently large to be detected after convolution with a thermal Gaussian profile (see solid curves). It is possible that a reduction of the assumed electron fraction in the CB00 model (by a factor of $\gtrsim 3$, in view of the results presented in Paper II) may improve the agreement with observations, but this needs verification.

Another way of looking at these data is to consider the mean velocity as determined from first moments of the intensity distribution. In Fig. 8, we compare the measured velocities as a function of offset along the major and minor axes of L 1544 with predictions from the simulation. Along the minor axis, we see that the models show a sharp gradient close to the center as one might expect intuitively for a radial infall model. This is most marked for intermediate inclinations (37°) since in pure edge-on models, one sees both red and blue-shifted gas with equal weight. Far from the center of the core, the contribution of gas at large radius (and low velocity) becomes large and the expected line of sight velocity decreases. Along the major axis in contrast, we expect at all inclinations no discernible relative velocity. Any gradients that are present must be due to other effects such as rotation.

We see from Fig. 8 that while there is reasonable agreement between the expected and observed velocity variation along the minor axis for N_2D^+ , there are clearly discrepancies for other species. And along the major axis to the SE, all species (including N_2D^+) show red-shifts contrary to model predictions. One could imagine that this latter effect was due to rotation except that transitions such as $\text{N}_2\text{H}^+(1-0)$ also show signs of red-shifts along the major axis to the NW.

Finally, there is a tendency for model lines to get broader toward the core center (factor of 1.5 from a projected distance of $40''$ to the center, see Fig. 6), in agreement with what observed (Fig. 5), although predicted line widths are significantly narrower than observed.

Our general conclusion from this set of comparisons is that contraction in the plane of an inclined disk as in the CB00 model is likely to be one element of a successful kinematical model. The simulation which we have made is certainly very crude and needs to be refined. A more realistic treatment of the abundance variation and molecular excitation would be one such refinement. However, we suspect also that a successful model will have a somewhat larger infall velocity and will take account of rotation.

4.2. MZ synthetic profiles and comparison with observed data

Since the MZ model is one dimensional, we did not attempt to use it to reproduce the variation of profiles along the minor axis. To compute the MZ line profile of $\text{HC}^{18}\text{O}^+(1-0)$ in Figure 9 we specify the vertical structure of the molecular density, the velocity dispersion, the settling speed, and the excitation temperature. We briefly summarize these relations here. We approximate the vertical density structure of the MZ layer as

$$n = \frac{n_0}{1 + (z/z_0)^2} \quad (1)$$

where n_0 is the central density and z_0 a characteristic scale height, given by

$$z_0 = \frac{(1 + R)\sigma_T^2}{(2\pi mGN)} \quad (2)$$

with m the mean molecular mass, G the gravitational constant, N the total column density, σ_T the thermal velocity dispersion, and R the squared ratio of the nonthermal and thermal velocity dispersions at the midplane. The central density is related to the column density by

$$n_0 = \frac{\pi G m}{2(1+R)} \left(\frac{N}{\sigma_T} \right)^2. \quad (3)$$

The molecular abundance n_{mol}/n is assumed to be depleted to zero in the central half of the layer, i.e. for $|z| < z_0$, and to be constant for $z \geq z_0$.

The nonthermal motions in the horizontal plane are due to Alfvén waves. The settling speed of the quasistatically condensing layer, at height z and at angle θ , is

$$v = -\frac{zR\Gamma\sin(\theta)}{1 + (3/2)R} \quad (4)$$

where Γ is the midplane dissipation rate of the turbulent motions. This rate depends on the physical basis of the dissipation, for which MZ adopt an MHD turbulent cascade, terminating in ion-neutral friction. In general the dissipation is a function of time. Here for simplicity we take Γ to be a constant, Γ_f , to be determined by the best fit of the model to the spectral line. With this assumption, the turbulence parameter R decreases with time t from its initial value R_i according to $R = R_i \exp(-\Gamma_f t)$.

The radiative transfer is computed assuming plane-parallel transmission of optically thin line radiation, in 8 layers from $z/z_0 = -7/4$ to $7/4$ in increments of $1/2$. The excitation temperature of the HC^{18}O^+ transition is modelled simply according to a two-level excitation model.

To obtain the fit shown in Fig. 9 we used the parameter values given in Table 4. For the parameters adopted in Table 4, the depletion zone has extent 1400 AU.

In choosing N we were guided, via eq. 3, by the requirements that the central temperature and density match those adopted in Paper II for the high-density core of L 1544, 10 K and $\sim 1 \times 10^6 \text{ cm}^{-3}$ respectively. The line width was fit by iteratively adjusting R , θ , and Γ . The line shape and height were set by N and on the combination of depletion and contraction.

We found that the model line profile is double-peaked only if the model has both depletion and contraction. The profile is single-peaked if the model has depletion but no contraction, or if it has contraction but no depletion.

Although the MZ model fits the observed central profile well, we caution that its application to the present problem is simplified for convenience so that the uniform dissipation rate Γ_f is a fit parameter and is not derived from a physical dissipation process. For the present parameter choices $1/\Gamma_f$ is comparable to the free-fall time from position z_0 to the midplane of the model layer. Thus Γ_f corresponds to dissipation which is about as fast as is physically allowable. More detailed modelling will be needed to make a more meaningful comparison.

5. Conclusions

This study has had as its main aim to study the high density core nucleus of L 1544. One important result is that, while many species including CO are depleted at densities of 10^5 or more, N_2H^+ and in particular N_2D^+ are less affected. N_2D^+ best traces the region where the dust continuum radiation peaks and hence the kinematics of N_2D^+ offer a guide to the dynamical behavior of the high density core. We were able to detect the 3–2 transitions of both N_2H^+ and N_2D^+ and do not see evidence for “collapse” in the observed profiles. However, this is in good part due to the difficulties caused by the blending of hyperfine satellites.

We see in several apparently optically thin lines a profile showing “double structure” towards the nucleus of L 1544. While we cannot exclude the presence of “self-absorption”, our data suggest that at high densities (above a few times 10^4 cm^{-3}), one observes two components with different velocities along the line of sight. Although there is no compelling proof, it seems likely to us that we are observing a foreground and a background layer of moderate density ($3 \cdot 10^4$ to 10^5 cm^{-3}) separated by the highest density gas from which all heavy species (with the possible exception of N_2) have depleted out. This relative motion between foreground and background could plausibly be the infall at a velocity of order 0.1 km s^{-1} discussed by CB00.

We have attempted to test this idea by comparing both observed profiles and mean velocities with those predicted by CB00. The observations show that those species which best trace the dust peak have a velocity gradient along the minor axis of L 1544. This feature of the data is reproduced by our simulations even if the real velocity field is clearly more complex than in the model. Part of the difference could be due to superimposed rotation but we regard the present evidence for this as unconvincing.

The model profiles also show double peaked profiles in the central position of the disk in rough agreement with those observed. Here however, the interpretation is difficult because there is good evidence that the profiles of low excitation transitions such as some of the $\text{N}_2\text{H}^+(1-0)$ satellites are affected by the foreground absorption mentioned above. We have attempted to minimise the importance of such effects using optically thin tracers in order to isolate the kinematics of the high density gas and get good qualitative agreement even if the model profiles are somewhat narrower than those observed. It is important to realise that models of this type in general predict “double-peaked” profiles of optically thin high density tracers along the major axes, in reasonable agreement with observations (see histograms in Fig. 6). In the CB00 model this is due to the disk-like structure seen almost edge on and contracting radially in the plane of the disk. Because of thermal line broadening, the double nature is maintained only at the center and if a central hole due to depletion is present.

Although the agreement between observations and CB00 model is not perfect, the above results in our opinion give support to the idea proposed by many authors (Shu et al. 1987, Mouschovias and Ciolek 1999 and references therein) that ambipolar diffusion is one of the basic processes of star formation. This is backed up by the results in Paper II which show that the

ionization degree in the core of L 1544 is sufficiently low that the ambipolar diffusion time scale and the free-fall time scale are of the same order.

Our data have also been compared with the MZ model. In Section 4.2 we saw that this model reproduces the line profile of an optically thin tracer observed towards the dust peak to within its noise. The success in reproducing the observed $\text{HC}^{18}\text{O}^+(1-0)$ line width is due to the inclusion of turbulent motions. As in the case of the CB00 model, the double peak structure is the result of depletion which removes gas at central positions and thus at central velocities, contributing to the dip in the line profile. Since the MZ model is horizontally uniform, it cannot be used in its present form to compare with the variation of line profiles in the plane of the sky. Nonetheless, the present result demonstrates that contraction along field lines toward a depleted high-density zone may provide a viable explanation for the observed profiles, suggesting that dissipation of Alfvénic turbulence is an important process for the dynamical evolution of prestellar cores.

The MZ model predicts that the nonthermal motions (and thus linewidths) get smaller as the gas gets denser. This is not what L1544 shows at its center (see Fig. 5). On the other hand, the CB00 model shows some line broadening towards the center (see Fig. 6), although linewidths are still significantly narrower than observed. From this we conclude that a combination of the two models is probably needed to best reproduce our data. In particular, we speculate that the densest part of L1544 has broader lines because it is in transition from 1D condensation along field lines (MZ model) to 3D condensation (1D along field lines as above, plus 2D across field lines via fast ambipolar diffusion as in CB00 model). The key ingredient which allows the ambipolar diffusion to approach the free-fall rate is the depletion which reduces the ambipolar diffusion time by reduction of the ion fraction. This point will be illustrated in Paper II.

The authors are grateful to the referee, Neal Evans, for useful comments and suggestions. PC and CMW wish to acknowledge travel support from ASI Grants 66-96, 98-116, as well as from the MURST project “Dust and Molecules in Astrophysical Environments”.

A. Frequencies for $\text{N}_2\text{H}^+(3-2)$, $\text{N}_2\text{D}^+(2-1)$, and $\text{N}_2\text{D}^+(3-2)$

Frequencies for the N_2H^+ and N_2D^+ transitions studied here have been computed on the basis of the molecular constants determined by Caselli et al. 1995. We assume that the quadrupole coupling constants for the inner and outer nitrogen atoms are identical for N_2D^+ and N_2H^+ and we neglect effects due to the presence of deuterium. This gives for N_2D^+ essentially the same hyperfine pattern as Gerin et al. 2001 tabulate for $\text{N}_2\text{D}^+(2-1)$ and $(3-2)$. There are then 45 separate components of the 3–2 lines for the two species and 38 for $\text{N}_2\text{D}^+(2-1)$. These have been used to fit the data shown in Fig. 2 where one sees that the approximation used is adequate. The blending is such however that we cannot improve the estimates for the hyperfine splitting. We have however checked that the rest frequencies used are accurate to within 0.1 km s^{-1} if one assumes the same velocity for $\text{N}_2\text{H}^+(3-2)$, $\text{N}_2\text{D}^+(2-1)$, $\text{N}_2\text{D}^+(3-2)$ as for $\text{N}_2\text{H}^+(1-0)$. We have also collected for reference in Table 1 the frequencies of the 16 $\text{N}_2\text{H}^+(3-2)$ transitions with more than 1 percent of the total line intensity. One sees from this that there is roughly 10 percent of the line intensity in the other 29 components.

REFERENCES

- Alves, J.F., Lada, C.J., Lada, E.F. 2001, *Nature*, 409, 159
- André P., Ward–Thompson D., Barsony M. 2000, in: *Protostars and Planets IV* (Book - Tucson: University of Arizona Press; eds Mannings, V., Boss, A.P., Russell, S. S.), p. 59
- Bacmann A., André P., Puget J. -L., Abergel A., Bontemps S., Ward–Thompson D. 2000, *A&A*, 361, 555 (BAP)
- Bergin E. A., Ciardi D. R., Lada C. J., Alves J., Lada E. A. 2001, *ApJ*, in press
- Bergin E. A., Langer W. D. 1997, *ApJ*, 486, 316
- Caselli P., Myers P. C., Thaddeus P. 1995, *ApJ*, 455, L77
- Caselli P., Walmsley C. M., Tafalla M., Dore L., Myers P. C. 1999, *ApJ*, 523, L165 (CWT99)
- Caselli, P., Walmsley C.M. 2001, in *From Darkness to Light*, eds Montmerle, T., André, P., in press
- Caselli P., Walmsley C. M., Zucconi A., Tafalla M., Dore L., Myers P. C. 2001, *ApJ*, submitted (Paper II)
- Ciolek, G.E., Basu S 2000 *ApJ* 529, 925 (CB00)
- Ciolek G.E., Basu S. 2001, in *From Darkness to Light*, eds Montmerle, T., André, P., in press

- Comito C., Caselli P., Walmsley C. M., Tafalla M., in preparation
- Dore L., Cazzoli G., Caselli P. 2001, *A&A*, 368, 712
- Evans N.J. II, Rawlings J.M.C., Shirley Y., Mundy L.G. 2001, *ApJ*, in press
- Frerking M.A., Langer W.D. 1981 *J. Chem. Phys.*, 74, 6990
- Gerin, M., Pearson J.C., Roueff E., Falgarone E., Phillips T.G. 2001, *ApJ*, 551, L193
- Goodman A. A., Barranco J. A., Wilner D. J., Heyer M. H. 1998, *ApJ*, 504, 223
- Goodman A. A., Benson P. J., Fuller G. A., Myers P. C. 1993, *ApJ*, 406, 528
- Gudeman C. S. 1982, PhD Thesis, University of Wisconsin, Madison
- Lovas F. J. 1992, *J. Phys. Chem. Ref. Data*, Vol. 2, No. 2, 181
- McKee C. F., Zweibel E. G. 1995, *ApJ*, 440, 686
- Mouschovias, T. Ch. & Ciolek, G.E. 1999 in *The Origin of Stars and Planetary Systems*. Edited by Charles J. Lada and Nikolaos D. Kylafis. Kluwer Academic Publishers, 1999, p.305
- Myers P. C., Zweibel E. G. 2001, *ApJ*, in press (MZ)
- Ohashi N., Lee S. W., Wilner D. J., Hayashi M. 1999, *ApJ*, 518, L41
- Penzias A. A. 1981, *ApJ*, 249, 518
- Pointer R. L., Pickett H. M. 1985, *Appl. Opt.*, 24, 2335
- Rawlings J. M. C., Hartquist T. W., Menten K. M., Williams D. A. 1992, *MNRAS*, 255, 471
- Shu F. H., Adams F. C., Lizano S. 1987, *ARA&A*, 25, 23
- Tafalla M., Mardones D., Myers P. C., Caselli P., Bachiller R., Benson P. J. 1998, *ApJ*, 504, 900
- Tafalla M., Myers P. C., Caselli P., Walmsley C. M., in preparation
- Ward–Thompson D., Motte F., André P. 1999, *MNRAS*, 305, 143 (WMA)
- Ward–Thompson D., Kirk J. M., Crutcher R. M., Greaves J. S., Holland W. S., André P. 2000, *ApJ*, 537, L135
- Williams J.P., Myers P.C., Wilner D.J., Di Francesco J. 1999 *ApJ*, 513, L61
- Zucconi A., Walmsley C.M., Galli D. 2001, *A&A*, in press

Table 1. Frequencies for $\text{N}_2\text{H}^+(3-2)$

$F'_1 F'$	$F_1 F$	Frequency MHz	Error MHz	Rel. Velocity ^a km s^{-1}	Rel. Intensity
3 4	3 4	279509.8785	0.0062	2.0120	0.0166
2 2	1 2	279511.1328	0.0064	0.6690	0.0154
2 2	1 1	279511.3445	0.0061	0.4424	0.0479
2 1	1 0	279511.3847	0.0061	0.3993	0.0222
3 3	2 3	279511.4305	0.0063	0.3503	0.0140
2 3	1 2	279511.5089	0.0062	0.2663	0.0945
3 3	2 2	279511.6858	0.0061	0.0769	0.0885
3 2	2 1	279511.7978	0.0061	-0.0430	0.0610
4 3	3 2	279511.8097	0.0061	-0.0557	0.1005
4 4	3 3	279511.8114	0.0061	-0.0576	0.1356
3 4	2 3	279511.8083	0.0061	-0.0542	0.1249
2 1	1 1	279511.8486	0.0063	-0.0974	0.0187
4 5	3 4	279511.8621	0.0061	-0.1118	0.1746
4 3	3 3	279512.3171	0.0065	-0.5990	0.0102
2 2	2 2	279514.2219	0.0063	-2.6385	0.0114
2 3	2 3	279514.3427	0.0063	-2.7678	0.0141

^aVelocities are relative to an assumed rest frequency of 279511.757 MHz

Table 2. Line parameters from gaussian fits to spectra taken at the (20,-20) offset.

Transition	Frequency MHz	Ref.	T_{mb} K	$\int T_{\text{mb}} dv$ K km s ⁻¹	V_{lsr} km s ⁻¹	Δv km s ⁻¹
HC ¹⁸ O ⁺ (1-0)	85162.222	1	0.35±0.05 0.39±0.05	0.07±0.01 0.09±0.01	7.04±0.01 7.28±0.01	0.18±0.03 0.23±0.03
H ¹³ CO ⁺ (1-0)	86754.279	1	1.7±0.2 1.1±0.2	0.33±0.03 0.24±0.03	7.03±0.01 7.39±0.01	0.24±0.02 0.20±0.03
HC ¹⁷ O ⁺ (1-0) ^a	87057.258	2	0.06±0.01 0.05±0.01	0.011±0.003 0.010±0.003	7.15±0.03 7.38±0.03	0.19±0.06 0.18±0.07
HN ¹⁵ N ⁺ (1-0) ^b	90263.833	3	< 0.047
N ₂ H ⁺ (1-0) ^c	93173.2650	4	1.96±0.05	0.83±0.01	7.154±0.003	0.397±0.006
C ¹⁸ O(1-0)	109782.1734	5	4.9±0.2	1.53±0.03	7.180±0.002	0.292±0.005
C ¹⁷ O(1-0)	112358.988	6	2.19±0.04	0.61±0.02	7.189±0.001	0.274±0.005
D ¹³ CO ⁺ (2-1)	141465.141	7	0.22±0.03 0.11±0.03	0.05±0.01 0.02±0.01	7.08±0.02 7.35±0.04	0.20±0.04 0.20±0.08
DCO ⁺ (2-1)	144077.321	3	3.1±0.1 1.0±0.1	0.88±0.06 0.49±0.06	7.098±0.001 7.37±0.03	0.271±0.008 0.46±0.05
DCO ⁺ (3-2)	216112.623	3	2.4±0.3 0.6±0.3	0.7±0.1 0.17±0.09	7.14±0.02 7.40±0.05	0.27±0.03 0.26±0.05
C ¹⁸ O(2-1)	219560.3568	5	4.4±0.8	2.0±0.2	7.19±0.02	0.43±0.04

^aValues refer to the main hyperfine component.

^bUpper limit based on assumed width of 0.3 km s⁻¹.

^cValues refer to the component $F_1, F = 0, 1 \rightarrow 1, 2$.

References: (1) Gudeman 1982; (2) Dore et al. (2001); (3) Lovas 1992; (4) Caselli et al. 1995; (5) Pointer & Pickett 1985; (6) Frerking & Langer 1981; (7) electronic Lovas catalogue; (8) Dore (priv. comm.)

Table 3. Line parameters from fits to the hyperfine structure of the $\text{N}_2\text{H}^+(1-0)$, $\text{N}_2\text{H}^+(3-2)$, $\text{N}_2\text{D}^+(2-1)$, and $\text{N}_2\text{D}^+(3-2)$ spectra taken at the (20,-20) offset^a

Transition	Frequency MHz	$\int T_{mb} dv$ K km s ⁻¹	T_{ex} K	V_{LSR} km s ⁻¹	Δv km s ⁻¹	τ
$\text{N}_2\text{H}^+(1-0)$	93173.4035 ^b	5.49±0.03	5.0±0.1	7.157±0.001	0.311±0.002	13.3±0.4
		5.15±0.01	4.90±0.09	7.162±0.001	0.304±0.001	13.8±0.2
$\text{N}_2\text{D}^+(2-1)$	154217.094 ^c	1.45±0.05	4.8±0.5	6.957±0.004	0.285±0.009	5.1±0.4
		1.72±0.02	4.6±0.3	6.968±0.002	0.287±0.005	4.0±0.2
$\text{N}_2\text{D}^+(3-2)$	231321.9063 ^d	0.49±0.04	...	7.04±0.01	0.31±0.03	0.1±0.2
		0.47±0.01	4±2	7.050±0.007	0.32±0.02	1.4±0.6
$\text{N}_2\text{H}^+(3-2)$	279511.9375 ^d	0.45±0.08	...	7.14±0.02	0.18±0.03	0±2
		0.67±0.04	4±1	7.117±0.009	0.16±0.02	6±2

^aParameters in first rows refer to the spectrum at (20,-20), whereas those in second rows are from the spectrum averaged over a 9×9 grid of positions, spaced by 10".

^bCentral line frequency from Caselli et al. 1995.

^cFrequency of the main hyperfine component ($F_1, F = 3, 2 \rightarrow 2, 3$), blended in the main group of hyperfines.

^dWeighted mean of hyperfines.

Table 4. Parameters Used for MZ Model Line Profile^a

R	θ (deg)	N (10 ²² cm ⁻²)	Γ_f (10 ⁻¹² s ⁻¹)	T (K)	v_0 (km s ⁻¹)
0.8	75	4.4	1.8	10	7.16

^a R is the midplane turbulence parameter, θ the angle between the vertical and the plane of the sky, N the total column density, Γ_f the best-fit constant turbulent dissipation rate, T the kinetic temperature, and v_0 the LSR velocity of the observed cloud.

Fig. 1.— Spectra of detected lines toward offset (20, -20), the “molecular peak”. From top to bottom: $\text{C}^{18}\text{O}(1-0)$, component $F = 5/2 \rightarrow 5/2$ of $\text{C}^{17}\text{O}(1-0)$, $\text{H}^{13}\text{CO}^+(1-0)$, $\text{DCO}^+(2-1)$, $\text{DCO}^+(3-2)$, component $F_1, F = 0, 1 \rightarrow 1, 2$ (*thin line*) and $F_1, F = 1, 0 \rightarrow 1, 1$ (*dashed line*) of $\text{N}_2\text{H}^+(1-0)$, $\text{HC}^{18}\text{O}^+(1-0)$, $\text{D}^{13}\text{CO}^+(2-1)$, and component $F = 5/2 \rightarrow 5/2$ of $\text{HC}^{17}\text{O}^+(1-0)$. Dotted line mark the V_{LSR} determined from the hfs fit of $\text{C}^{17}\text{O}(1-0)$ ($= 7.189 \text{ km s}^{-1}$, see Tab. 2).

Fig. 2.— Histogram spectra of $\text{N}_2\text{H}^+(3-2)$, $\text{N}_2\text{D}^+(2-1)$, and $\text{N}_2\text{D}^+(3-2)$ towards the molecular peak of L 1544. An average has been made of the spectra towards offset (20,-20) and at 8 positions offset by 10-15 arc seconds relative to (20,-20) (i.e (10,-30) (20,-30) (30,-30) (10,-20) ...). We also show (solid curve) fits to the hyperfine structure of these lines made using the parameters discussed in the appendix.

Fig. 3.— Integrated intensity maps of $\text{DCO}^+(2-1)$, $\text{DCO}^+(3-2)$, $\text{H}^{13}\text{CO}^+(1-0)$, $\text{N}_2\text{H}^+(1-0)$, $\text{N}_2\text{D}^+(2-1)$, and $\text{N}_2\text{D}^+(3-2)$ overlapped to the 1.3mm continuum emission map from WMA smoothed at a resolution of $22''$ (*grey scale*). Contour levels are 30, 50, 70, and 90% of the peak [1.3 K km s^{-1} , for $\text{DCO}^+(2-1)$ at offset (20, -20); 0.8 K km s^{-1} for $\text{DCO}^+(3-2)$ at (20, -20); 0.8 K km s^{-1} for $\text{H}^{13}\text{CO}^+(1-0)$ at (0, -20); 5.5 K for $\text{N}_2\text{H}^+(1-0)$ at (20, -20); 2.1 K km s^{-1} for $\text{N}_2\text{D}^+(2-1)$ at (20, -20); 0.6 K for $\text{N}_2\text{D}^+(3-2)$ at (30, -20)]. The peak of the 1.3 mm map is $225 \text{ mJy}/22''$ at offset (26, -21). Note that all integrated intensity maps, in particular the $\text{N}_2\text{D}^+(3-2)$ one, have a peak nearby the dust peak, unlike the $\text{C}^{17}\text{O}(1-0)$ map (see CWT99).

Fig. 4.— Velocity gradient vectors in the plane of the sky derived from our 30-m maps of L 1544. We show from the top left going clockwise maps of $\text{DCO}^+(2-1)$, $\text{DCO}^+(3-2)$, $\text{N}_2\text{H}^+(1-0)$, $\text{N}_2\text{D}^+(3-2)$, $\text{N}_2\text{D}^+(2-1)$, $\text{H}^{13}\text{CO}^+(1-0)$. The integrated intensity maps of Fig. 3 are in the background. The thick arrows at the bottom right of each map shows velocity gradients averaged over the map and the numbers give the magnitudes of the gradients in km/s/pc . The thin arrows over the map show the magnitude (their length is proportional to the corresponding magnitude, in units of the total gradient magnitude) and direction of the velocity gradients derived from 9 neighbouring point regions across the maps where $T_{\text{mb}}/\sigma_{T_{\text{mb}}} > 3$. Points show the measured positions. With the exception of $\text{N}_2\text{D}^+(3-2)$, which best traces the contracting high density L1544 nucleus, all the other lines show complex velocity fields which cannot be simply ascribed to solid body rotation and infall.

Fig. 5.— Measured line widths in $\text{N}_2\text{H}^+(1-0)$, $\text{N}_2\text{D}^+(2-1)$, $\text{N}_2\text{D}^+(3-2)$, $\text{DCO}^+(2-1)$, and $\text{DCO}^+(3-2)$ plotted against the distance from the L 1544 “molecular peak”. The N_2H^+ and N_2D^+ measurements shown have been corrected for hyperfine blending. Note the slight fall off of the N_2H^+ and N_2D^+ linewidths with distance from (20, -20) offset indicative of infalling motions towards the core center.

Fig. 6.— Model profiles of an optically thin satellite of the $\text{N}_2\text{H}^+(1-0)$ line shown as a function of map offset for a model disk having the density distribution described by CB00 for time t_3 , with an inner hole of radius $r_h = 0.01 \text{ pc}$ (2100 AU). The velocity scale (in km s^{-1}) is reported for the

spectrum at offset (40, -20). The solid profiles take into account the line broadening due to thermal velocity dispersion for a temperature of about 10 K, while the histograms are purely kinematic. The disk like structure is supposed inclined by an angle of 16° to the line of sight and model profiles have been convolved with a beam of $24''$. The x-axis of this figure is supposed to represent the major axis of the disk and the y-axis the minor axis. Adjacent model spectra are separated by $20''$. The (0,0) position in this model map corresponds to the (20,-20) offset in Fig. 3.

Fig. 7.— CB00 model (curve) and observed profiles (histogram) of the $\text{N}_2\text{H}^+ F_1, F = 1, 0 \rightarrow 1, 1$ satellite along the minor axis of L 1544. Model profiles are obtained with an inner hole as in Fig. 6. Offsets are given in arc seconds in the top right corner of each panel. The normalization of the intensity scale is arbitrary. The peak of the observed hyperfine shows a shift from blue to red going from north-east to south-west across the minor axis, correctly reproduced by the CB00 model, although model linewidths are narrower than observed.

Fig. 8.— Cuts showing the mean line of sight velocity derived from the model profiles similar to those of Fig. 6 as a function of offset on the sky. Both for the models and data, we have used the velocity determined from first moments of the intensity distribution. The panels show the expected and observed velocities for cuts along the major axis (right) and the minor axis (left). Measurements are shown by the error bars. Model curves for the minor axis are plotted for inclinations of 70° (dotted), 37° (dashed) and 16° (full). For the major axis, the CB00 model predicts no velocity offset (full horizontal line). Note the good agreement between the model and observed velocity profile along the minor axis for the N_2D^+ lines, which best trace the dense and highly CO-depleted nucleus of the core.

Fig. 9.— Comparison of MZ model line profile (smooth curve) and $\text{HC}^{18}\text{O}^+(1-0)$ spectrum (histogram) from L1544 position (20, -20). The MZ model is based on a self-gravitating layer which condenses quasistatically along magnetic field lines as it dissipates its Alfvénic turbulence. The model parameters are described in Table 4 and are discussed in the text. The MZ model reproduces the linewidth and the line profile substantially better than the CB00 model, although it cannot be used for studies of line variation across the core.

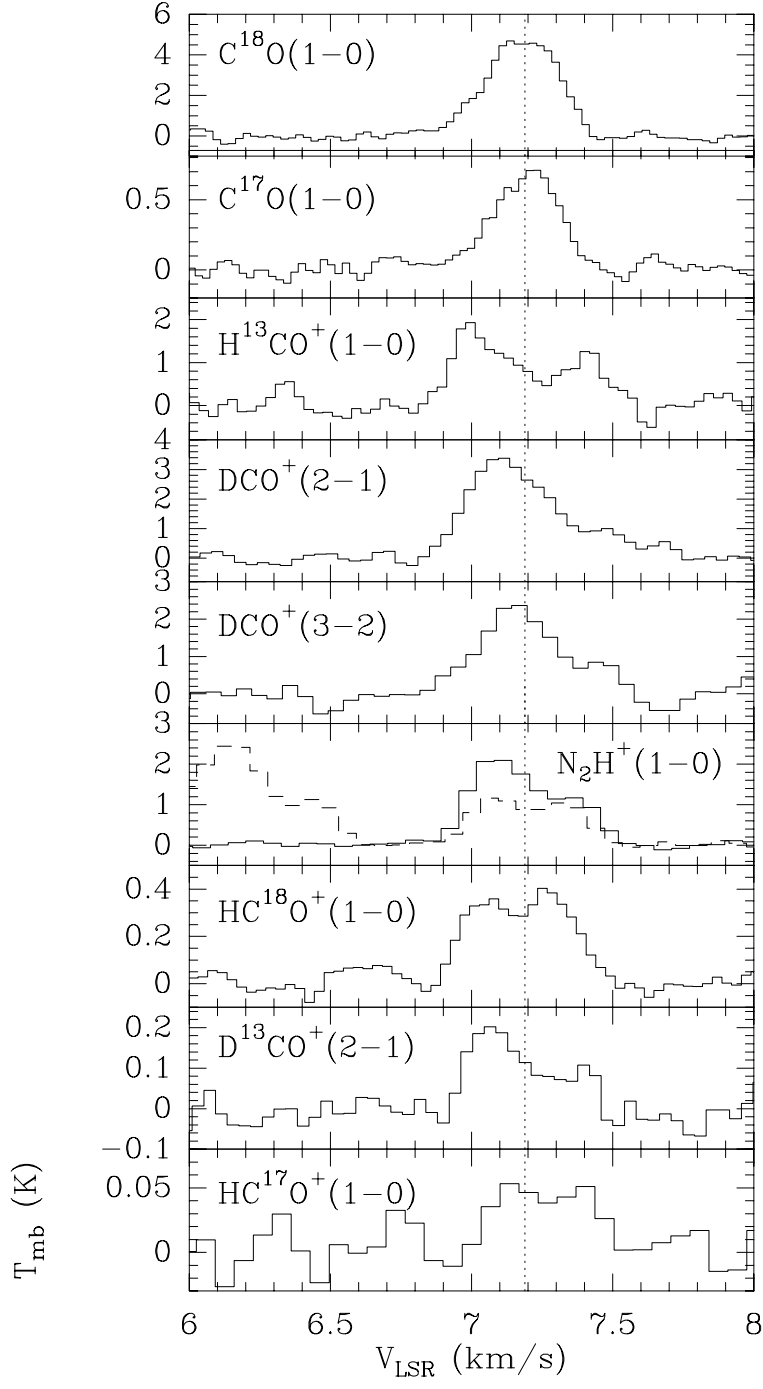


Fig.1

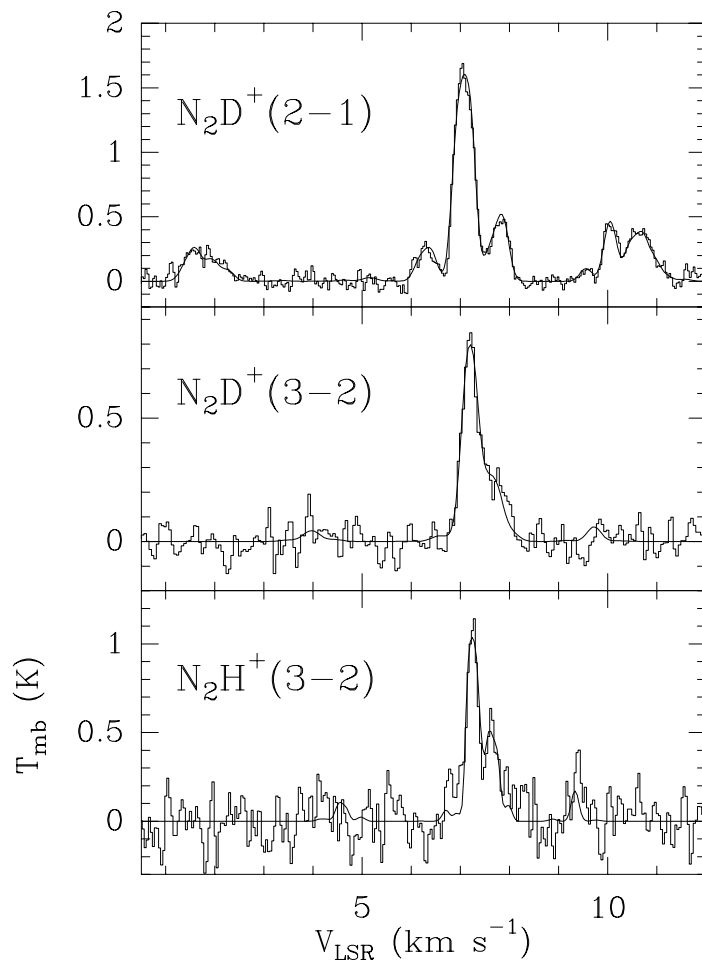


Fig.2

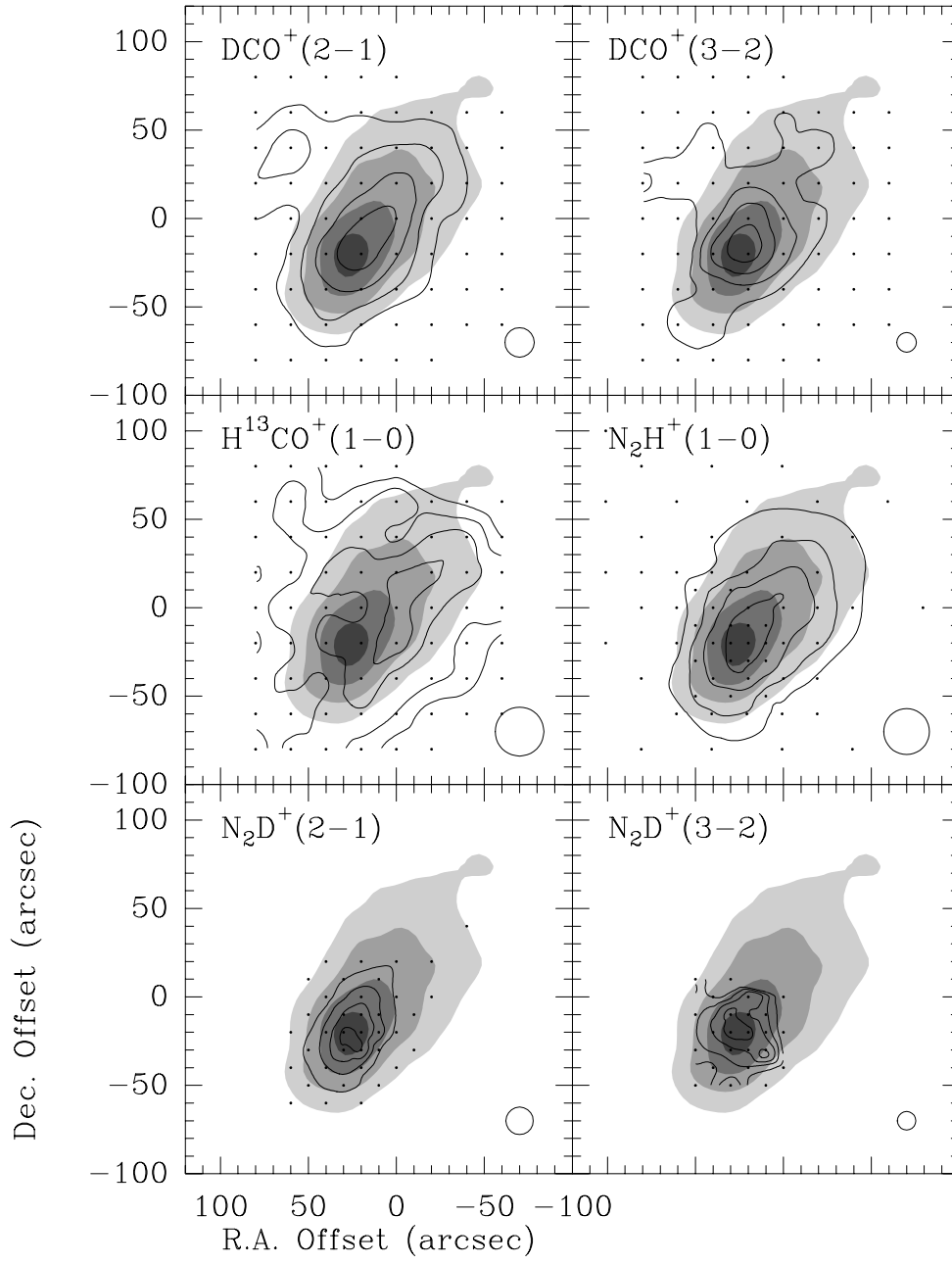


Fig.3

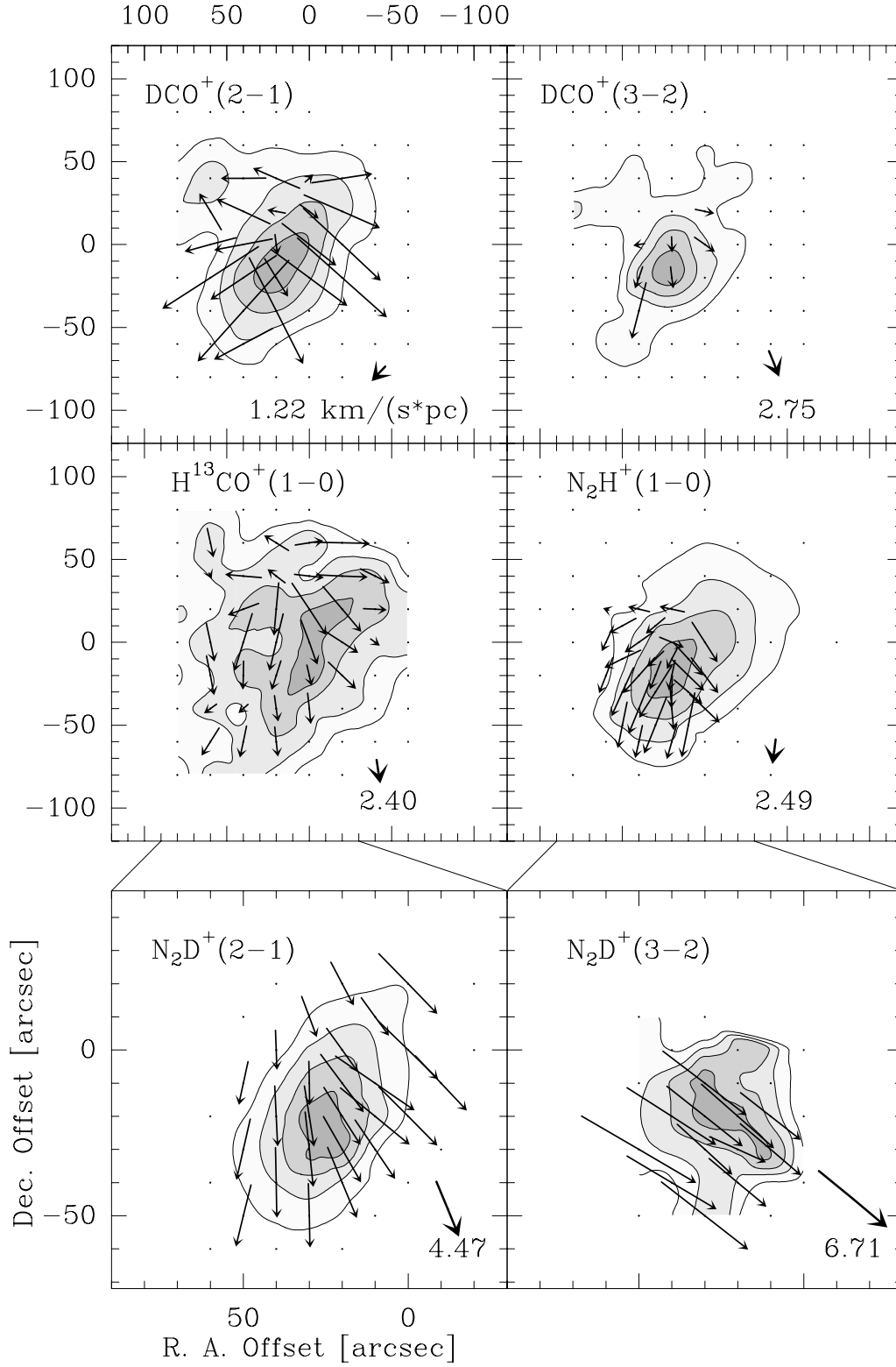


Fig.4

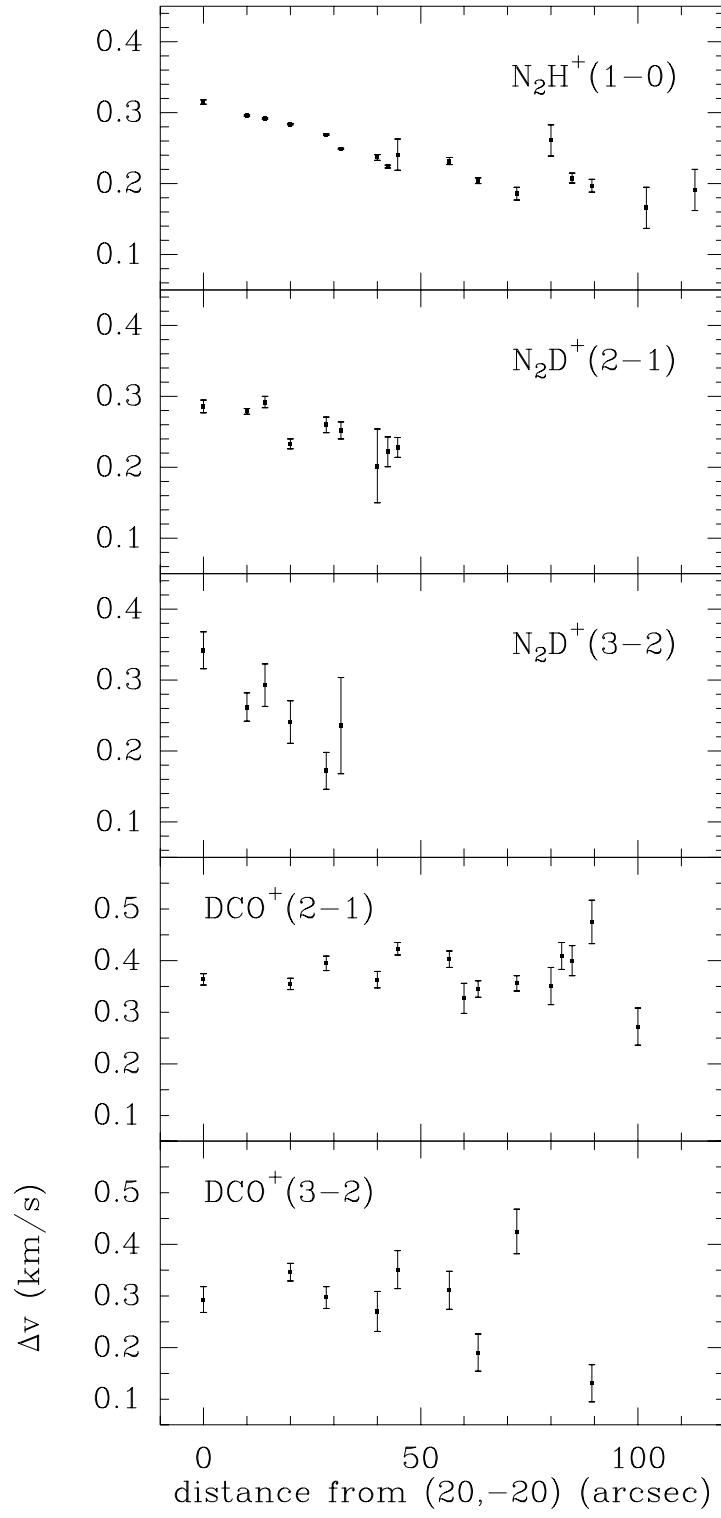


Fig.5

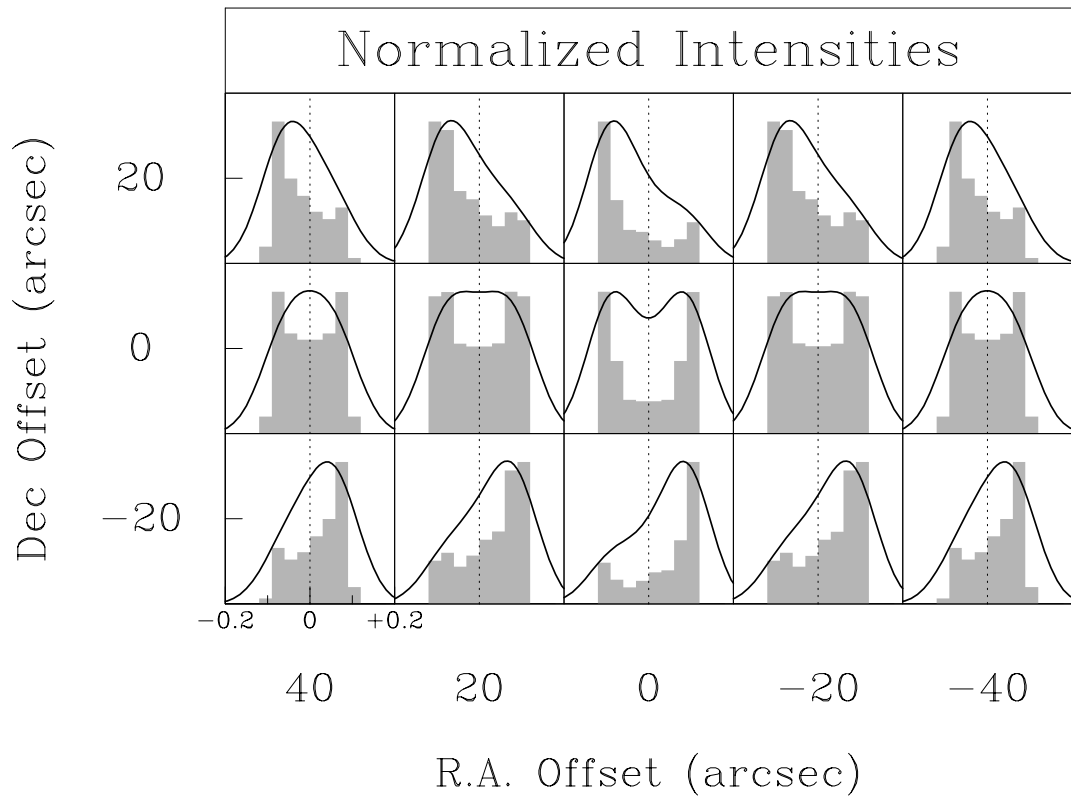


Fig.6

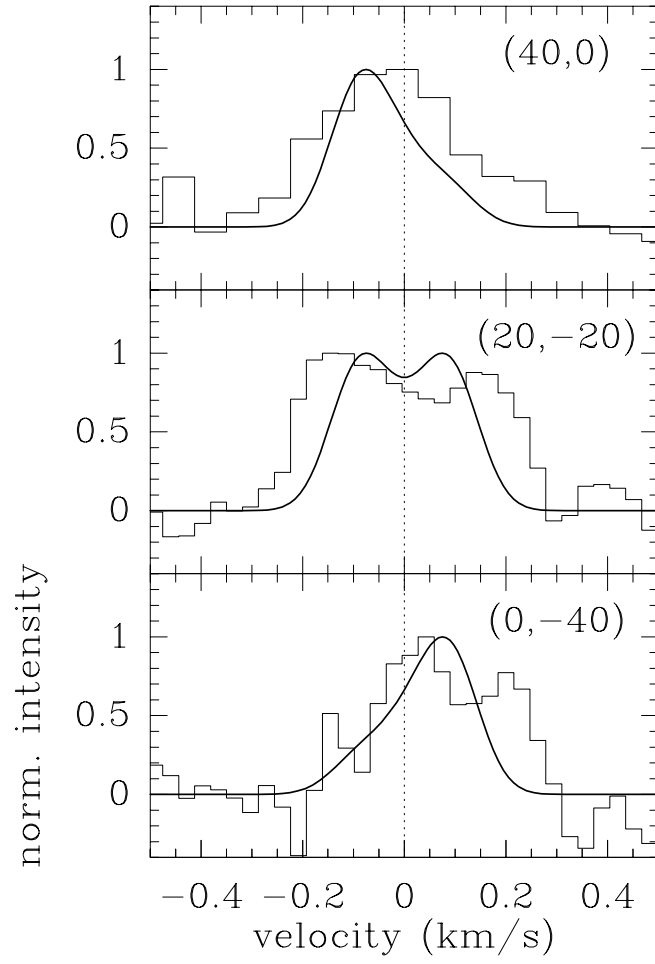


Fig.7

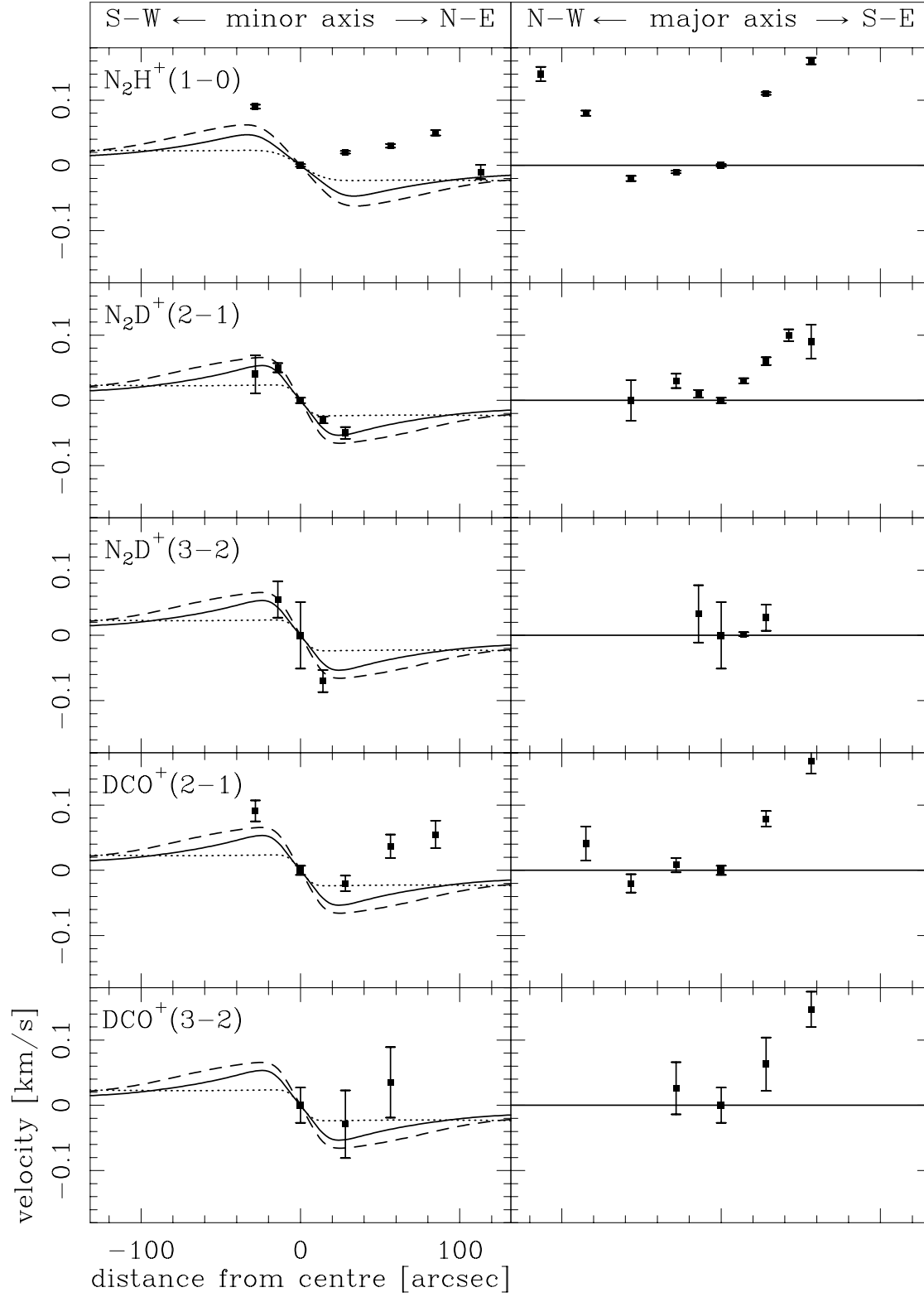


Fig.8

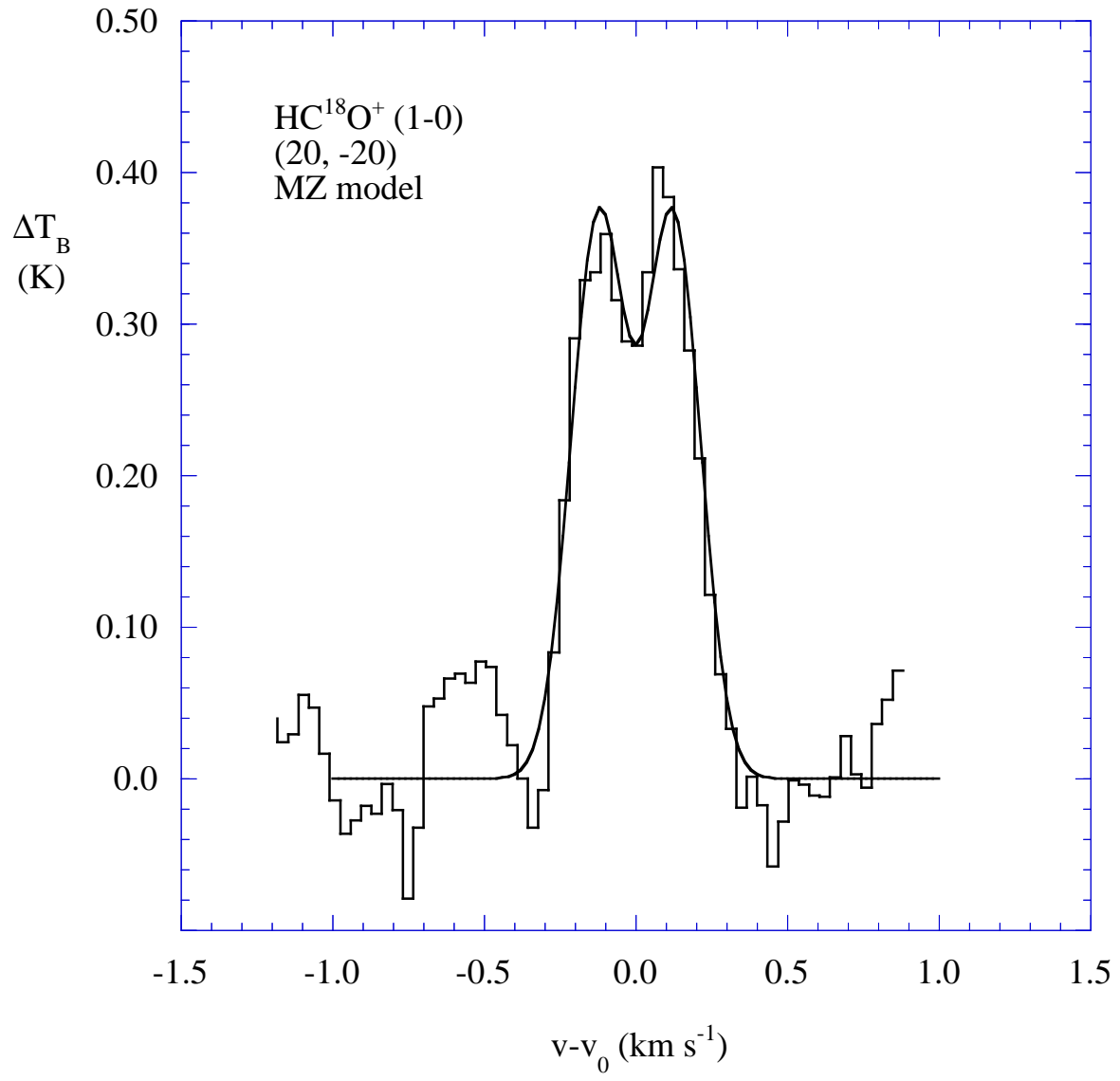


Fig.9